

## Frontiers

## Conservative generalized bifurcation diagrams and phase space properties for oval-like billiards



Diogo Ricardo da Costa <sup>a,b,\*</sup>, André Fujita <sup>b</sup>, Antonio Marcos Batista <sup>c,d</sup>,  
Matheus Rolim Sales <sup>d</sup>, José Danilo Szezech Jr <sup>c,d</sup>

<sup>a</sup> Department of Physics, Federal University of Paraná, CEP Curitiba/PR, 80060-000, Brazil

<sup>b</sup> Department of Computer Science, Institute of Mathematics and Statistics, University of São Paulo, CEP São Paulo/SP, 05508-090, Brazil

<sup>c</sup> Department of Mathematics and Statistics, State University of Ponta Grossa, CEP Ponta Grossa/PR, 84030-900, Brazil

<sup>d</sup> Graduate in Science Program - Physics, State University of Ponta Grossa, CEP Ponta Grossa/PR, 84030-900, Brazil

## ARTICLE INFO

## Article history:

Received 21 April 2021

Revised 1 December 2021

Accepted 2 December 2021

Available online 20 December 2021

## Keywords:

Oval-like billiards

Nonlinear dynamics

Chaotic system

CGBD plot

## ABSTRACT

In this paper, we study some dynamic properties for oval-like billiards. These billiards have two control parameters, named  $\epsilon$ , which controls the deformation of the boundary, and  $p$ , which changes the number of inflection points. The particle's position  $(X, Y)$  uses Cartesian coordinates, and the angle  $\mu$  gives us the particle's direction. Here we consider a Poincare section, where we calculate the position  $X$  (in the horizontal axis) and angle  $\mu$  every time a particle crosses  $Y = 0$  (in the vertical axis). We compute the phase space and the conservative generalized bifurcation diagrams (CGBD). These diagrams are obtained when changing the initial position  $X$  and the control parameter  $\epsilon$ . We plot the respective maximum Lyapunov exponent for each combination of the control parameter and initial condition, which uses a customized color palette. These diagrams show how complex billiards dynamics are, where one can find the direct and inverse parabolic bifurcations. Moreover, one can highlight periodic, quasi-periodic, and chaotic regions. We found a fractal behavior (self-similar structure), where we verified the existence of period-adding structures logical sequences (periodic orbits) in the CGBD. These sequences accumulate in different regions depending on the control parameters, following the main body's period and accumulating in different regions. When we set the control parameter  $p$  to 1, we observe that chaos dominates for a high enough value of the control parameter  $\epsilon$  (which controls our billiard's deformation). We also studied some orbits embedded in stochastic layers that appear near saddle points, which obey another period-adding logical sequence. These stochastic layers play a crucial role in the dynamics of billiard systems because that chaos grows in such regions, near saddle points, after increasing the control parameter's value.

© 2021 Elsevier Ltd. All rights reserved.

### 1. Introduction

The study of billiards is an important research field in dynamical systems. We define a billiard as a closed domain bordered by a hard wall, in which we introduce a point-like particle [1–9]. The main idea is to have a simple class of models, which shows the complicated behavior of non-integrable smooth Hamiltonian systems without integrating a differential equation. By connecting the dynamics with geometry, billiards correspond to models that qualitatively mimic various complex systems' properties, mechanisms, or effects. Depending on the boundary's shape, we can observe regular [1,4,5], mixed [6–9], or fully chaotic dynamics

[10–12]. It can be considered both classical [1,4–12] and quantum [13–15] versions, as well as relativistic particles [16,17]. Several different billiards can be studied. We find some applications in physical problems, such as superconducting and confinement of electrons in semiconductors by electric potentials [18,19], ultracold atoms trapped in a laser potential [20,21], mesoscopic quantum dots [22,23], the reflection of light from mirrors [24,25], waveguides [26,27], and microwave billiards [22,28,29]. Other examples of billiards can also be cited, for instance, elliptical [30,31], stadium [11], and mushroom [7–9].

When we talk about billiards, one can cite studies that show a semiclassical transition from an elliptical to an oval billiard [32]. It is also possible to study the semiclassical treatment of diffraction in billiard systems with a flux line [33]. Another interesting study shows the influence of corners in billiard systems, as done in Ref [34]. Reference [32] is specially important because shows

\* Corresponding author.

E-mail address: [diogo.costa@unesp.br](mailto:diogo.costa@unesp.br) (D.R. da Costa).

some examples of bifurcations that occur in billiard systems. One goal of our paper is to explore some of these bifurcations, focusing on the direct and inverse parabolic bifurcations that occur in oval-like billiards.

We are going to consider a modified version of an oval-like billiard [1,3,6,35–37]. We demonstrate that two control parameters can completely change the dynamics of the system. In Section 2, we show details about the model and describe some essential initial considerations. Our intention here is to explore some conservative generalized bifurcation diagrams (CGBD) [31,35,38,40], where we go deeper into the study of these structures. These diagrams are composed of trees whose main stems are the periodic orbits (resonances) and infinite ramifications, which are all rational tori (higher-order resonances) surrounding the periodic orbits [38]. The CGBD plots are important because one can find the direct and inverse parabolic bifurcations. One can also highlight periodic, quasi-periodic, and chaotic regions. To find the linear stability of the fixed points, one could use some methods, like Greene's residue [39], but, when using the CGBD, one can visually identify where the periodic orbits lose linear stability or duplicate.

We show period-adding structures that have a non-trivial pattern that depends on the system and control parameters chosen. Our main contribution relies on the fact that, for billiards, one can obtain the value of  $K/L$ , where  $K$  refers to the number of times the particle reached the Poincaré section, i.e., the number of times in which the trajectory crossed  $Y = 0$ . The second number  $L$  refers to the number of hits with the billiard boundary. With this in mind, we show some period-adding sequences of structures that appear and accumulate in different regions. We also show several examples of trajectories to explain these periodic structures.

In Sections 3 and 4, we present results for different control parameters' values. We find some unusual orbits that are embedded in stochastic layers. These layers appear near saddle points, which is the mechanism for creating chaos in the system. We present final remarks in Section 5.

## 2. The model and considerations

Let  $\theta \in [0, 2\pi)$  and  $\epsilon \in [0, 1)$  be the angular position and amplitude of the deformation, respectively. Then, we write the radius of the billiard boundary in polar coordinates as

$$R(\theta) = 1 + \epsilon \cos(p\theta). \quad (1)$$

For  $\epsilon = 0$ , a circle billiard is recovered. The Cartesian position of the boundary is given by

$$X_b(\theta) = R(\theta) \cos(\theta), \quad (2)$$

$$Y_b(\theta) = R(\theta) \sin(\theta). \quad (3)$$

Fig. 1(a) displays a sketch of the billiard boundary for  $p = 2$  and  $\epsilon = 0.2$ . We consider that the particle starts its motion at  $(X, Y) = (X_0, Y_0)$ , wherein a first moment  $Y_0 = 0$ . The particle's trajectory makes an angle  $\mu_0$ , measured counterclockwise from the horizontal line. Although the trajectory propagates clockwise, its angle is measured counterclockwise. Let  $V_0$  be the initial particle's velocity and  $\Delta t$  be the time variation. Then, the position of the particle  $(X_p, Y_p)$  is given by:

$$X_p = X_0 + V_0 \cos(\mu_0) \Delta t, \quad (4)$$

$$Y_p = Y_0 + V_0 \sin(\mu_0) \Delta t. \quad (5)$$

For simplicity, we set  $V_0 = 1$ . We can also write the particle's trajectory as

$$Y_p = Y_0 + \tan(\mu_0)(X_p - X_0). \quad (6)$$

To identify the interception of the particle's trajectory with the billiard boundary, we solve a transcendental equation, considering  $(X_b(\theta_1), Y_b(\theta_1)) = (X_p, Y_p)$ . After that, we find the new angular position  $\theta_1$  in which the particle touches the boundary. The particle's trajectory is specularly rejected with constant velocity.

Every time the particle's trajectory crosses  $Y = 0$ , we annotate the position  $X$  of the interception and the angle  $\mu$ . For example, Fig. 1(a) shows that the particle intercepts  $Y = 0$  in  $X_1$  and  $X_2$  with angles  $\mu_1$  and  $\mu_2$ . Therefore, the green dashed line (represented by  $Y = 0$ ) is the Poincaré section. Figs. 1(b) and 1(c) display billiard boundaries for  $p = 1$  and  $p = 2$ , respectively. We change the value of  $\epsilon$  from 0 (circular boundary) to 0.9. Let  $\epsilon_c = \frac{1}{1+p^2}$ , then the billiard has some local negative curvatures when  $\epsilon > \epsilon_c$ .

As we will show in the next sections, the dynamical properties are highly dependent on  $\epsilon$  and  $p$ .

## 3. Results for $p = 1$

To verify if an orbit is chaotic, we can use a critical observable named Lyapunov exponent [41]. It is a practical tool that can quantify the average expansion or contraction rate of a small volume of initial conditions. Let  $J_i$  be the Jacobian matrix evaluated over an orbit that hits  $n$  times the billiard boundary and  $\Lambda_j$  be the eigenvalues of  $M = \prod_{i=1}^n J_i$ . Then, the Lyapunov exponents [41] are defined as

$$\lambda_j = \lim_{n \rightarrow \infty} \frac{1}{n} \ln |\Lambda_j|, \quad j = 1, 2. \quad (7)$$

In our simulations, we consider orbits that hit up to  $10^4$  times the billiard boundary. If  $\lambda \rightarrow 0$ , the orbit may have periodic behavior, while for  $\lambda \gg 0$ , the orbit may present chaotic behavior.

Let us introduce the Conservative Generalized Bifurcation Diagram (CGBD). These diagrams exhibit the location and different bifurcations (inverse and direct parabolic bifurcations [31]), without the necessity of calculating, for example, the Greene's Residue [39]. It contains infinite sub-diagrams with all rational/irrational tori from the periodic orbits. Results are remarkable and show self-similar and generic bifurcation structure in conservative systems. Fig. 2 displays CGBD plots for  $p = 1$ . Due to the symmetries, we consider  $\mu_0 = \pi/2$  to construct the CGBD plots and change  $X_0$  and  $\epsilon$ 's values. It is fair to say that when considering  $\alpha = \pi/2$ , it is possible to lose some periodic orbits that exist in different regions of the phase space. However, due to the symmetry of this billiard, some periodic islands appear at the line  $\alpha = \pi/2$ . It is correct to say that this is a particular case, but we will still get similar behavior, with the fractal behavior, when choosing other control parameters combinations. If we take another value of  $\alpha$ , it is still possible to see similar results, but slightly changed.

In our simulations, we consider 1 000 different values of  $X_0$  and 1 000 different values of  $\epsilon$ . For each pair  $(X_0, \epsilon)$ , we iterate an orbit until it hits  $10^4$  times the billiard boundary and compute the Lyapunov exponent  $\lambda$ . We use a specific color palette to represent  $\lambda$ , highlighted at the top of Fig. 2. Regions with  $\lambda \rightarrow 0$  tend to have blue or black colors, while higher values of  $\lambda$  are represented by red, orange, or white colors. The white regions typically highlight chaotic orbits, while black regions represent periodic motions.

The periodic structures are located mainly in regions with low  $\epsilon$  values, as shown in Fig. 2. We see that chaos dominates the dynamics for  $\epsilon > 0.5$ , i.e., almost all periodic islands are destroyed (losing linear stability). It is essential to observe that  $X_0 \in (X_{\min}, X_{\max})$ , where  $[X_{\min}, X_{\max}] = [X_b(\pi), X_b(0)]$ . The black-colored regions in the left of  $X_{\min}$  and  $X_{\max}$ 's right are regions not allowed (with no physical meaning because the particle is outside the billiard boundary).

Fig. 2 (b) exhibits an enlargement in the orange rectangle B shown in Fig. 2(a). We show, with more details, the apparent frac-

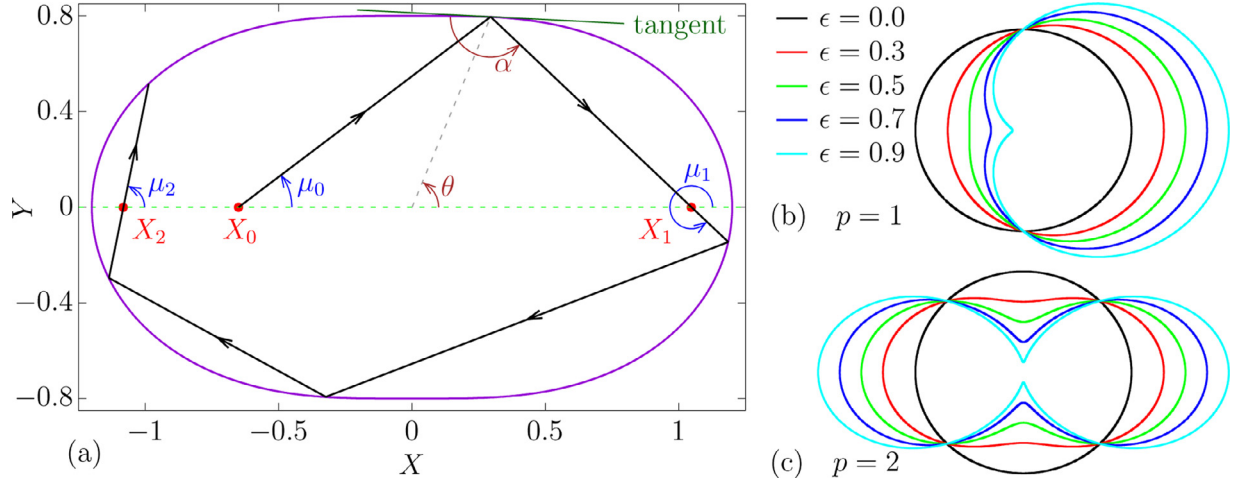


**Fig. 1.** (Color online) Sketch of an oval-like billiard, wherein item (a) we show an example of trajectory starting at  $(X_0, Y_0) = (-0.65, 0)$ . We set the control parameters as  $p = 2$  and  $\epsilon = 0.2$ . Angle  $\mu_0$  gives us the particle direction. In (b,c), we show billiard boundaries for different values of  $\epsilon$ , wherein item (b)  $p = 1$  while in (c)  $p = 2$ .

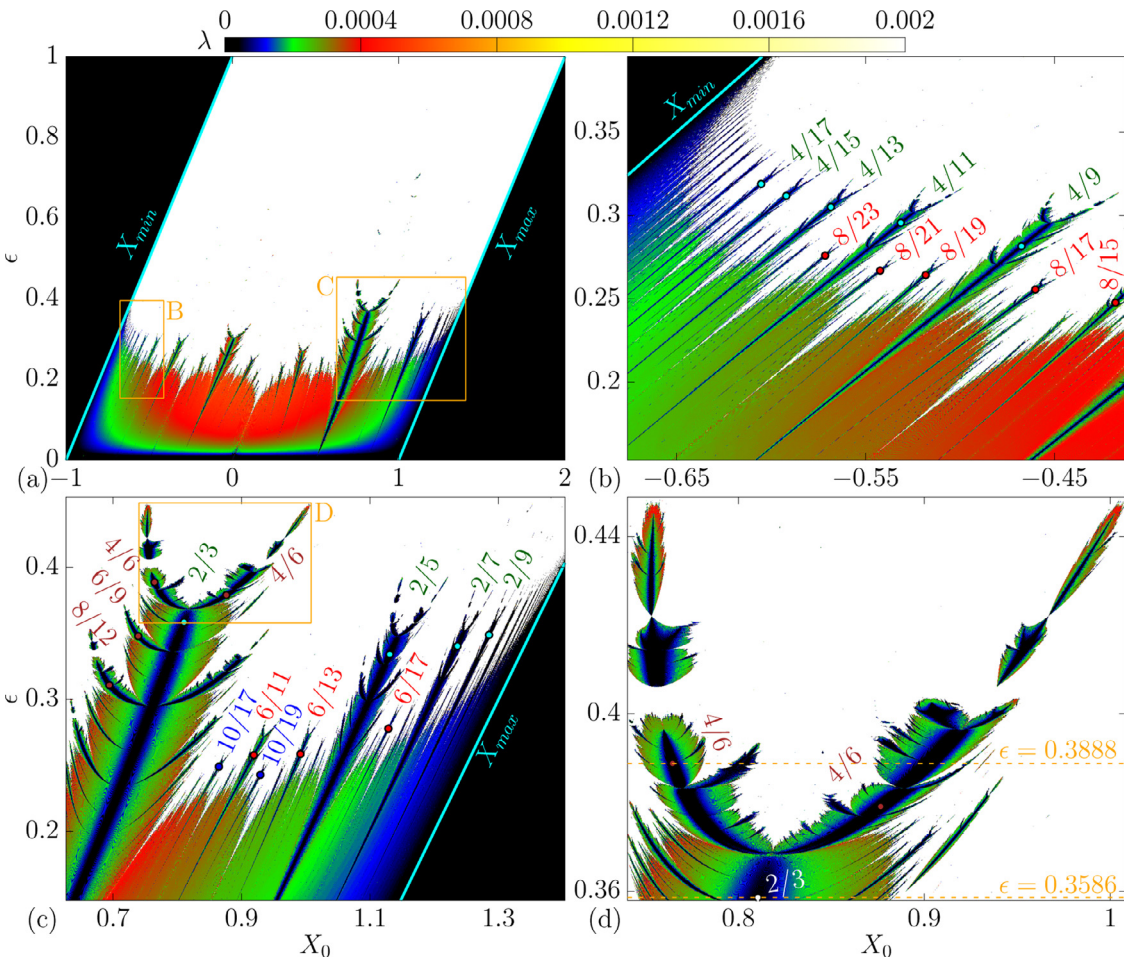


**Fig. 2.** (Color online) CGBD for  $p = 1$  and  $\mu_0 = \pi/2$ . The palette color shows the maximum Lyapunov exponent  $\lambda$ . We see numbers  $K/L$  separated by bars, where the first number  $K$  refers to the number of times the particle reached the Poincaré section, while the second number  $L$  refers to the number of hits with the billiard boundary.

tal behavior of the CGBD. There is a clear organization pattern of the periodic structures. In this figure, we see numbers  $K/L$  separated by bars, where the first number  $K$  refers to the number of times the particle reached the Poincaré section, i.e., the number of times in which the trajectory crossed  $Y = 0$ . In contrast, the second number  $L$ , refers to the number of hits with the billiard boundary. For example, let us take the conditions that produce the trajectory

$K/L \equiv 4/9$  in Fig. 2(b), represented by the little cyan circle in the coordinate  $(X_0, \epsilon) = (-0.4674, 0.2816)$ . Fig. 3(a) shows the correspondent trajectory. To count the number of times that a particle crosses  $Y = 0$ , we start in the second red circle (from left to right). For  $\mu_0 = \pi/2$ , the particle's trajectory goes vertically to the top. In a clockwise direction, we count the number of times it crosses  $Y = 0$  until returning to the initial point. It reaches our Poincaré

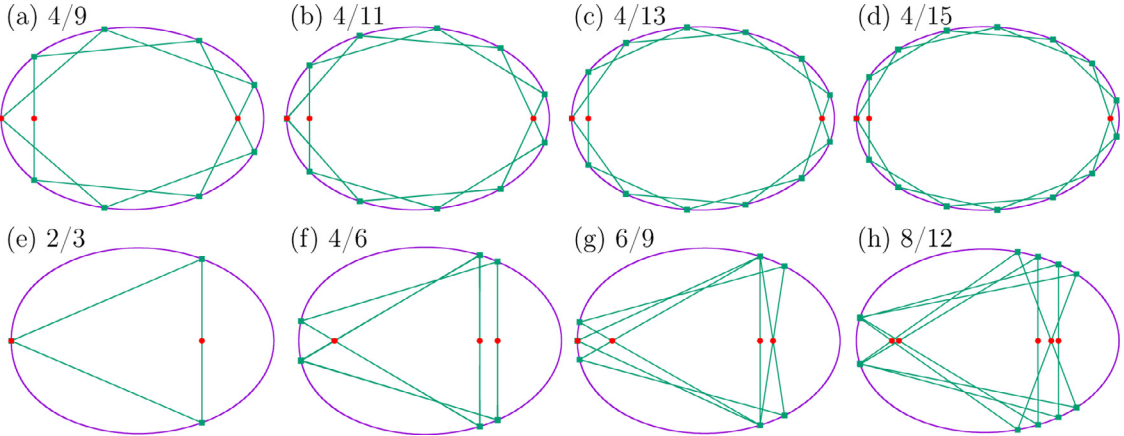


**Fig. 3.** (Color online) Examples of periodic trajectories for  $p = 1$ . Trajectories in (a,b,c,d) are examples taken from Fig. 2(b), representing rotational motion, while (e,f,g,h) are shown in Fig. 2(c), representing librational motion. The numbers separated by bars ( $K/L$ ) represent the number of times the particle reached the Poincaré section and the number of hits with the billiard boundary.

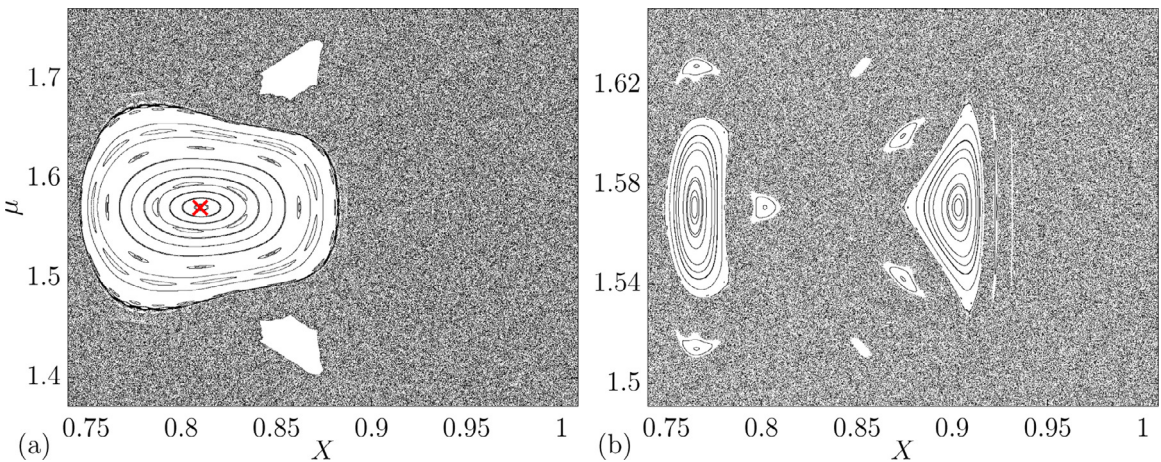


**Fig. 4.** (Color online) Phase space for  $p = 1$  and: (a)  $\epsilon = 0.3586$ ; (b)  $\epsilon = 0.3888$ . After a critical value, the island in (a) duplicates, creating the islands shown in (b).

section 4 times ( $K = 4$ ). However, it hits the billiard boundary nine times ( $L = 9$ ) before returning to the initial point. Then, this trajectory is represented by  $4/9$ . It is essential to observe that this is a periodic behavior.

Returning to Fig. 2(b), we see trajectories that follow an interesting pattern. For example, we identify trajectories with  $K/L$  given by  $4/9, 4/11, 4/13, 4/15, 4/17$ , and so on. We add two units for the value of  $L$  while  $K$  remains equal to 4. This period-adding sequence converges infinitely to  $X_{\min}$ . We observed a similar sequence for  $K = 8$ , where we see trajectories with  $K/L$  equal to  $8/15, 8/17, 8/19$ , and so on.

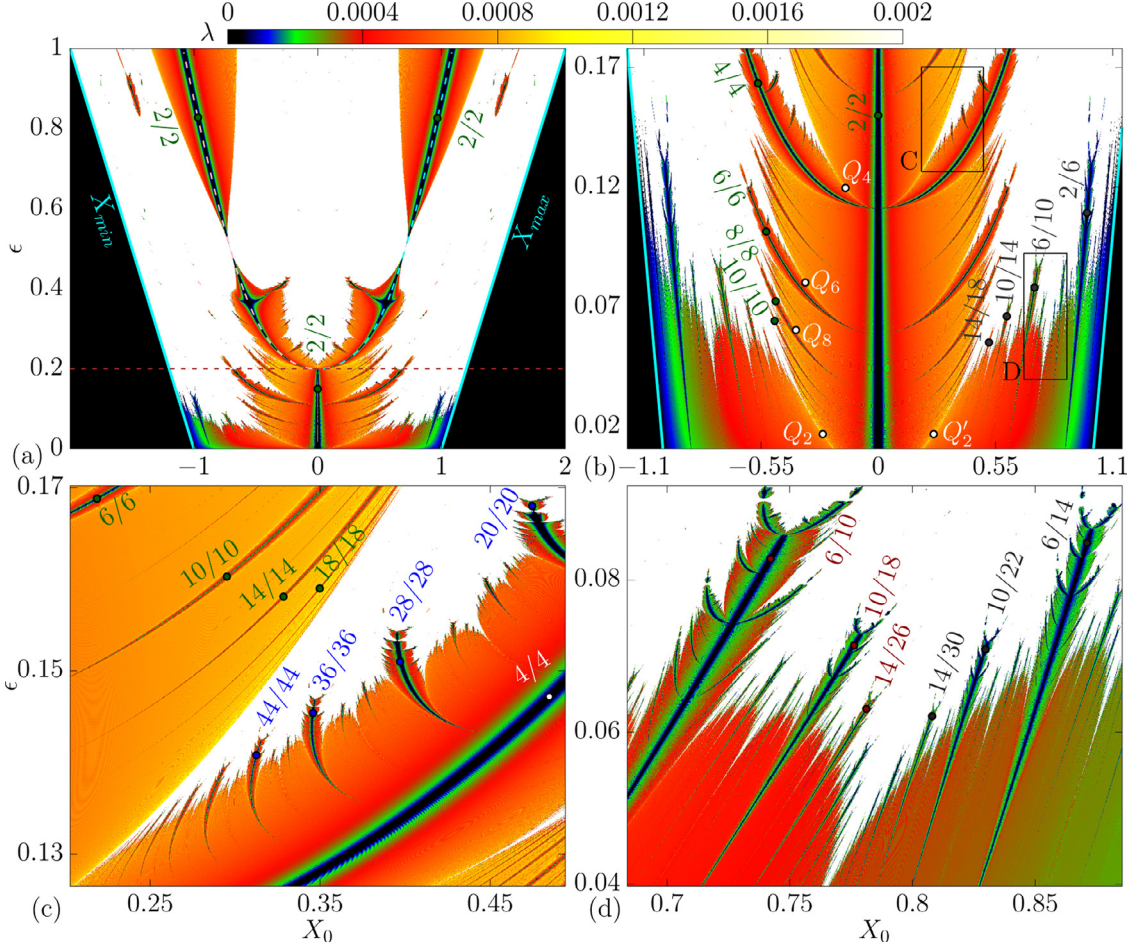
Fig. 2(c) shows an enlargement in the C region shown in Fig. 2(a). Here we see other period-adding sequences, where we highlighted a sequence with constant values of  $K = 2$  ( $2/3, 2/5, 2/7, 2/9, \dots$ ),  $K = 6$  ( $6/11, 6/13, 6/17, \dots$ ), and  $K = 10$  ( $10/17, 10/19, \dots$ ). All these period-adding sequences with constant  $K$  accumulate in  $X_{\max}$ . In the left corner of Fig. 2(c), we see another sequence, now with  $K/L$  given by  $4/6, 6/9, 8/12$ , and so on. It adds two units to  $K$  and three units to  $L$ , i.e., it follows the period of the main structure  $2/3$ . Figure 2(d) displays details inside the D rectangle shown in Fig. 2(c). We find that the periodic fixed point  $2/3$  loses the linear stability (becomes unstable/hyperbolic), and two branches  $4/6$  are created.

Fig. 3 shows examples of periodic trajectories. The trajectories  $4/9, 4/11, 4/13$ , and  $4/15$  (rotational motion) are taken from the little cyan circles in Fig. 2(b). In contrast, the trajectories  $2/3, 4/6, 6/9$ , and  $8/12$  (librational motion) are taken as the little brown

circles in Fig. 2(c). We are observing specifically Figs. 3(e) and 3(f), the trajectory  $2/3$  lost linear stability and created two  $4/6$  trajectories, as explained in Fig. 2(d).  $\epsilon = 0.3586$  and  $\epsilon = 0.3888$  are the values of  $\epsilon$  taken to construct the trajectories in Figs. 3(e) and 3(f). Altogether, Figs. 4(a) and 4(b) display the corresponding phase space  $\mu$  vs  $X$ , where each point represents the position and angle in which the particle crosses  $Y = 0$  (our Poincaré section). Fig. 4(a) exhibits a periodic island, wherein the center (red cross) has a fixed point with  $K/L = 2/3$ . As  $K = 2$ , we can say that this is a period-2 fixed point, which means that we can observe another similar island in other regions of the phase space. However, for visual purposes, we decide to highlight only this one. After a critical  $\epsilon$  value, the island in Fig. 4(a) duplicates, creating the islands shown in Fig. 4(b). The separation between these two islands increases when  $\epsilon$  increases. It can be observed in Fig. 2(d) by the two branches that started to separate for higher  $\epsilon$  values. When  $\epsilon$  is slightly greater than 0.44, the two branches (or the two periodic islands shown before) lose linear stability, i.e., the islands in Fig. 4(b) will disappear. For greater values of  $\epsilon$ , the chaos starts dominating the dynamics.

#### 4. Results for $p = 2$

Fig. 5 (a) shows the CGBD for  $p = 2$  and  $\mu_0 = \pi/2$ . For  $\epsilon < \epsilon_c = 0.2$ , a fixed point located at  $X_0 = 0$  ( $K/L = 2/2$ ) is stable, but it loses the linear stability for  $\epsilon > \epsilon_c$  and becomes unstable (hyperbolic).



**Fig. 5.** (Color online) CGBD for  $p = 2$  and  $\mu_0 = \pi/2$ . The color palette shows the maximum Lyapunov exponent  $\lambda$ . We see numbers  $K/L$  separated by bars, where the first number  $K$  refers to the number of times the particle reached the Poincaré section, while the second number  $L$  refers to the number of hits with the billiard boundary.

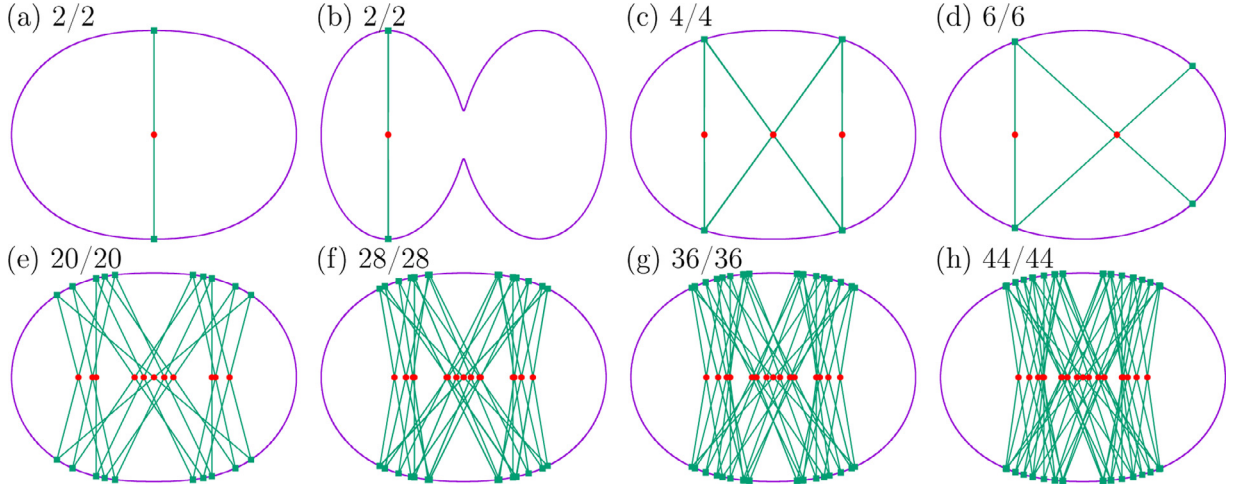


**Fig. 6.** (Color online) Examples of periodic trajectories for  $p = 2$ . Trajectories in (a,b) are examples taken from Fig. 5(a), while (c,d) are shown in Fig. 5(b) and (e,f,g,h) are shown in Fig. 5(c). The numbers separated by bars ( $K/L$ ) represent the number of times the particle reached the Poincaré section and the number of hits with the billiard boundary, respectively.

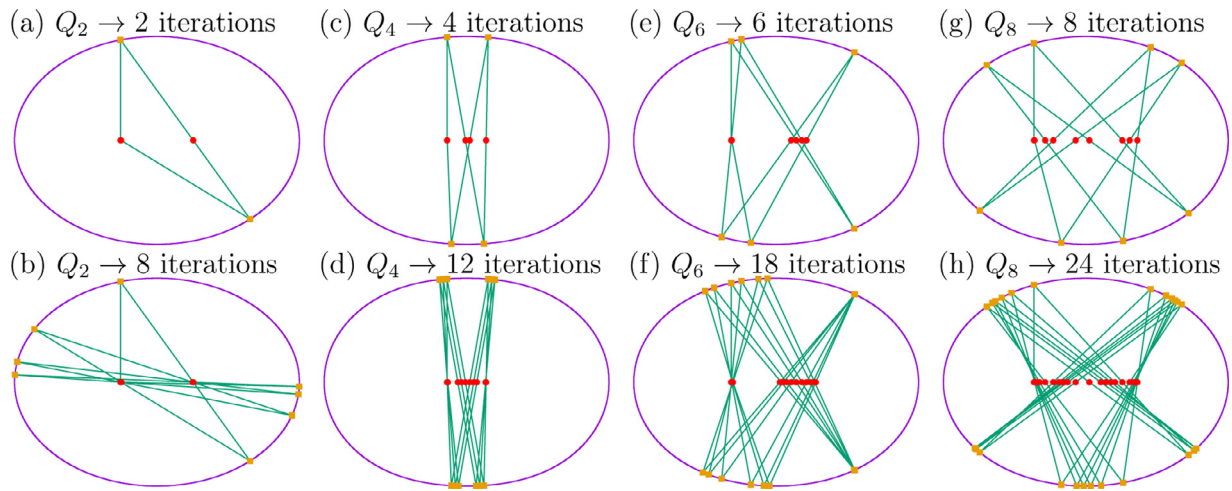
For  $\epsilon > 0.2$ , two different fixed points are created, both with  $K/L \equiv 2/2$  as well, and there is not a period-doubling bifurcation.

Fig. 6 (a) exhibits the trajectory  $2/2$  before  $\epsilon < \epsilon_c$ , while Fig. 6(b) displays one of the trajectories  $2/2$  created for  $\epsilon > \epsilon_c$ . It touches the boundary in two distinct positions. One at a maximum (named as  $Y_m$ ) and another at a minimum value of  $Y$ . We can find

$Y_m$  by solving  $\partial Y_b / \partial \theta = 0$ , which leads to the following transcendental equation

$$F(\theta) = -\epsilon p \sin(p\theta) + X_b(\theta), \quad (8)$$

that needs to be solved numerically for  $F(\theta_m) = 0$ . In addition to that, one can find  $[X_m, Y_m] = [X_b(\theta_m), Y_b(\theta_m)]$ , which gives us



**Fig. 7.** (Color online) Examples of quasi-periodic trajectories for  $p = 2$ . These are examples taken from Fig. 5(b).

the coordinate of the Y's maximum value. For  $p = 2$  and  $\epsilon > \epsilon_c$ , two maximums, and two minimum values can be found. Fig. 5(a) shows the values of  $X_m$  found as dashed lines. In both branches, the period-2 fixed points momentarily lose the linear stability at  $\epsilon \approx 0.5$ , i.e., the periodic islands almost disappear but recover the linear stability for higher  $\epsilon$  values.

Fig. 5 (b) shows details of the main  $K/L = 2/2$  structure observed around  $X_0 = 0$ . On the left, we observe a sequence of period-adding structures named  $4/4, 6/6, 8/8, 10/10$ , and so on. We add two units to the value of  $K$  and  $L$ , where the value of  $K$  is equal to  $L$ , following the period of the main structure. We can

see another more complex sequence in the right, where we see the period-adding sequence  $2/6, 6/10, 10/14, 14/18, \dots$ . Here, the value of  $K$  differs from  $L$ . We add four units to  $K$  as well to  $L$ . Fig. 5(c) displays an enlargement in the C rectangle shown in Fig. 5(b). Our intention here is to show details around the  $4/4$  structure. As shown in Fig. 5(c), we verify a period-adding sequence starting from  $20/20$ . The next structures have periods  $28/28, 36/36, 44/44, \dots$ , which accumulate near the figure's left-bottom corner. Another period-adding sequence is observed in the top-left corner, named as  $6/6, 10/10, 14/14, 18/18, \dots$ , which accumulate in the white region (chaotic region). We identify a fractal behavior

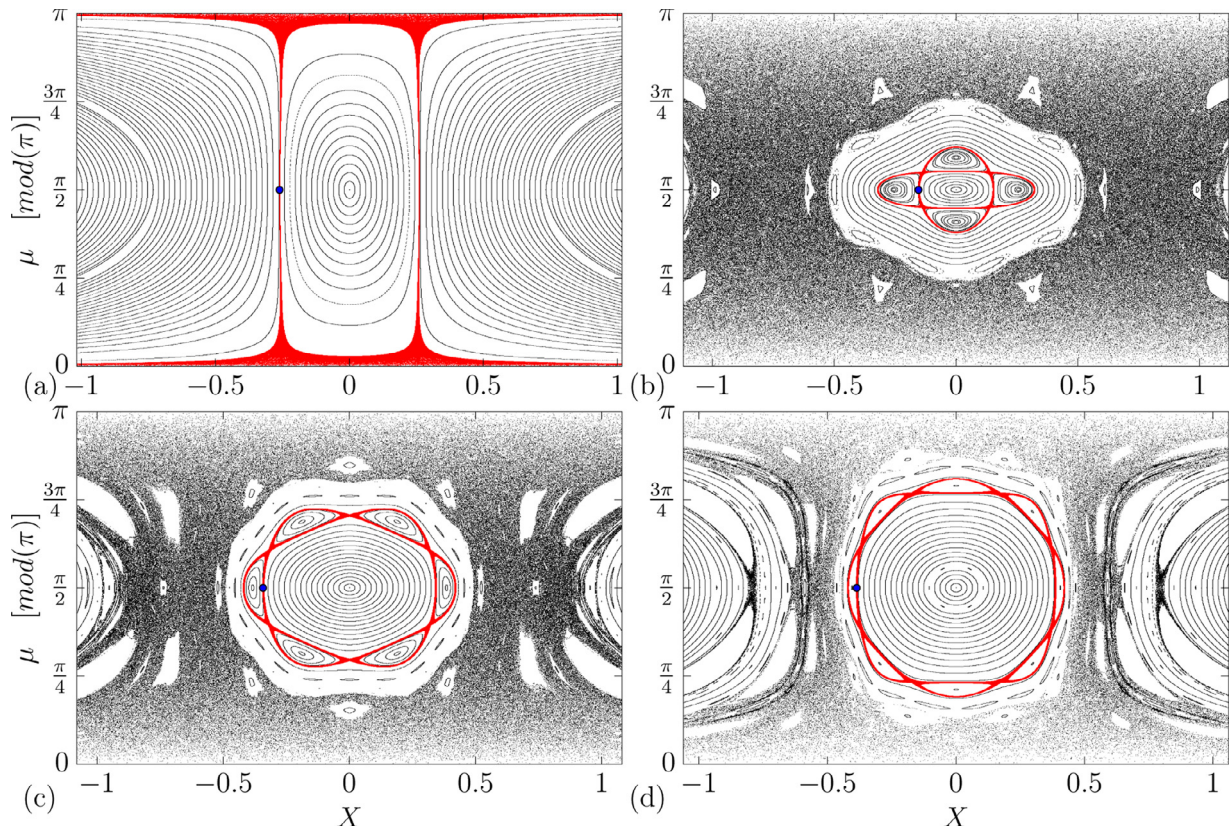


**Fig. 8.** (Color online) Examples of stochastic layers that appear for  $p = 2$ . The blue points in (a,b,c,d) represent, respectively, the initial conditions taken in  $Q_2, Q_4, Q_6$  and  $Q_8$  shown in Fig. 5(b). The value of  $\epsilon$  for each panel is: (a)  $\epsilon = 0.0169$ ; (b)  $\epsilon = 0.1197$ ; (c)  $\epsilon = 0.08025$ ; (d)  $\epsilon = 0.06038$ . The  $X$  position of the red circles (all with  $Y = 0$ ) is: (a)  $X_0 = -0.26019$ ; (b)  $X_0 = -0.1535$ ; (c)  $X_0 = -0.34169$ ; (d)  $X_0 = -0.38594$ . (For interpretation of the references to colour in this figure legend, the reader is referred to the web version of this article.)

(self-similar structures) that appears when successive zooms in are done.

After applying an enlargement in the D rectangle shown in Fig. 5(b), we obtain Fig. 5(d). We see more complex period-adding sequences appearing. For instance, we find the sequence 6/10, 10/18, 14/26, ... in the left and the sequence 6/14, 10/22, 14/30, ... in the right portion of the figure. Both sequences accumulate to the same point, where we add four units to  $K$  and eight units to  $L$ .

Fig. 6 shows examples of trajectories for  $p = 2$ . As said before, Figs. 6(a) and 6(b) exhibits examples taken from Fig. 5(a) before and after  $\epsilon_c$ . The trajectories 4/4 and 6/6 in Figs. 6(c) and 6(d) are taken from Fig. 5(b). The trajectories 20/20, 28/28, 36/36, and 44/44 in Figs. 6(e), 6(f), 6(g), and 6(h) are taken from Fig. 5(c), where we highlight the evolution of the trajectories that follow the period-adding sequence.

Observing again Fig. 5(b), we highlight some special regions, named  $Q_2$ ,  $Q_4$ ,  $Q_6$ , and  $Q_8$ . We explore the white regions that appear around the orange/red structures. For example, the trajectory  $Q_2$ , in Fig. 5(b), is highlighted in Fig. 7(a). As one sees, this trajectory starts at the left red circle, goes straight up (because  $\mu_0 = \pi/2$ ), reaching twice the billiard and the Poincaré section. The trajectory returns to the initial point after two iterations with our Poincaré section. However, the final angle is not the same as the original ( $\mu_2 \neq \pi/2$ ). Suppose we evolve this trajectory, for instance, for eight iterations. In that case, we see that the particle's trajectory returns to the initial after every two iterations. That is why we named  $Q_2$ , where the index represents the number of iterations until apparently returning to the initial point. Fig. 7(c) displays the trajectory  $Q_4$  shown in Fig. 5(b). This trajectory is not periodic because the angle when returning to the initial point is wrong. Fig. 7(d) shows the evolution for 18 iterations. The trajectory  $Q_6$  is shown in Figs. 7(e) and 7(f) for 6 and 18 iterations. Finally, the trajectory  $Q_8$  is observed in Figs. 7(g) and 7(h) when iterating up to 8 and 24 times. The trajectories ( $Q_j$ ) are very special and occur for some special combinations of the control parameters and initial conditions.

Let us consider the control parameters and initial conditions that produce  $Q_2$ ,  $Q_4$ ,  $Q_6$ , and  $Q_8$ . We can plot the complete phase space  $\mu$  vs  $X$ , shown in Figs. 8(a), 8(b), 8(c), and 8(d). The trajectories  $Q_2$ ,  $Q_4$ ,  $Q_6$ , and  $Q_8$  start in the blue circle, and these trajectories are embedded in stochastic layers. The layers are regions where chaos starts emerging. When the value of the control parameter  $\epsilon$  is increasing, the surrounding periodic structures are continuously destroyed. These stochastic layers [30] are created near the saddle points (hyperbolic fixed point). The creation of those stochastic layers can explain why white regions (with high  $\lambda$  values) appear near  $Q_j$  in Fig. 5(b).

## 5. Conclusions

In this paper, we explore conservative generalized bifurcation diagrams (CGBD), as well as phase space properties. These diagrams show how complex billiards dynamics are, where one can find duplication of the period, direct and inverse parabolic bifurcations. Moreover, one can highlight periodic, quasi-periodic, and chaotic regions. These plots display initial conditions versus non-linear parameters, and the color palette identifies the maximum Lyapunov exponent. In our simulations, we observe that periodic structures are organized in period-adding logical sequences, following the main body's period and accumulating in different regions. The structures shown have a fractal pattern. We obtained results for  $p = 1$  and  $p = 2$ , but our results can be extrapolated to other  $p$  values. For  $p = 1$ , we verify that chaos dominates the dynamics for high enough values of  $\epsilon$ . For  $p = 2$ , we highlighted some unusual orbits that are embedded in stochastic layers. These layers are essential to the dynamics because that chaos grows in

such regions (near saddle points) after increasing the control parameter's value. In summary, the CGBD plot shows essential details about the dynamics of billiard systems.

## Declaration of Competing Interest

The authors declare that they have no known competing financial interests or personal relationships that could have appeared to influence the work reported in this paper.

## CRediT authorship contribution statement

**Diogo Ricardo da Costa:** Conceptualization, Methodology, Software, Formal analysis, Writing – original draft. **André Fujita:** Validation, Formal analysis, Writing – review & editing. **Antonio Marcos Batista:** Validation, Formal analysis, Writing – review & editing. **Matheus Rolim Sales:** Validation, Formal analysis, Writing – review & editing. **José Danilo Szezech Jr:** Validation, Formal analysis, Writing – review & editing.

## Acknowledgments

This study was possible by partial financial support from the following Brazilian government agencies: Fundação Araucária, National Council for Scientific and Technological Development (CNPq), Coordenação de Aperfeiçoamento de Pessoal de Nível Superior-Brasil (CAPES), and São Paulo Research Foundation (FAPESP). DRC acknowledges Brazilian agencies FAPESP (2020/02415-7) and CNPq (162944/2020-9).

## References

- [1] Berry MV. Regularity and chaos in classical mechanics, illustrated by three deformations of a circular 'billiard'. *Eur J Phys* 1981;2:91.
- [2] Bunimovich LA. Physical versus mathematical billiards: From regular dynamics to chaos and back. *Chaos* 2019;29:091105.
- [3] Oliveira DFM, D Leonel E. On the dynamical properties of an ellipticaloval billiard with static boundary. *Commun Nonlinear Sci Numer Simulat* 2010;4:1092–102.
- [4] Garcia R. Elliptic Billiards and Ellipses Associated to the 3-Periodic Orbits. *Am Math Mon* 2019;126:491–504.
- [5] Bandres MA, Gutiérrez-Vega JC. Classical solutions for a free particle in a confocal elliptic billiard. *Am J Phys* 2004;72:810–17.
- [6] Hansen M, Costa DRd, Caldas II, Leonel ED. Statistical properties for an open oval billiard: An investigation of the escaping basins. *Chaos, Solitons & Fractals* 2018;106:355–62.
- [7] Bunimovich LA. Mushrooms and other billiards with divided phase space. *Chaos* 2001;11:802–8.
- [8] Bäker A, Ketzmerick R, Löck S, Robnik M, Vidmar G, Höhmann R, Kuhl U, Stöckmann HJ. Dynamical Tunneling in Mushroom Billiards. *Phys Rev Lett* 2008;100:174103.
- [9] Costa DRd, Palmero MS, Méndez-Bermúdez JA, Iarosz KC, Szezech JD Jr, Batista AM. Tilted-hat mushroom billiards: Web-like hierarchical mixed phase space. *Commun Nonlinear Sci Numer Simulat* 2020;91:105440.
- [10] Sinai YG. On the foundations of the ergodic hypothesis for a dynamical system of statistical mechanics. *Dokl Akad Nauk* 1963;153:1261–4.
- [11] Bunimovich LA. Conditions of stochasticity of two-dimensional billiards Q17. *Chaos* 1991;1:187–93.
- [12] Robnik M. Classical dynamics of a family of billiards with analytic boundaries. *J Phys A: Math Gen* 1983;16:3971–86.
- [13] Zanetti FM, Vicentini E, Luz MGEd. Eigenstates and scattering solutions for billiard problems: A boundary wall approach. *Ann Phys* 2008;323:1644–76.
- [14] Barnett AH, Betcke T. Quantum mushroom billiards. *Chaos* 2007;17:043125.
- [15] de Menezes DD, Silva MJ, de Aguiar FM. Numerical experiments on quantum chaotic billiards. *Chaos* 2007;17:023116.
- [16] Deryabin MV, Pustyl'nikov LD. Generalized relativistic billiards. *Regul Chaotic Dyn* 2003;8:283–96.
- [17] Deryabin MV, Pustyl'nikov LD. Exponential Attractors in Generalized Relativistic Billiards. *Comm Math Phys* 2004;248:527–52.
- [18] Dembowksi C, Gräß H-D, Heine A, Hofferbert R, Rehfeld H, Richter A. First Experimental Evidence for Chaos-Assisted Tunneling in a Microwave Annular Billiard. *Phys Rev Lett* 2000;84:867–70.
- [19] Bird JP. Recent experimental studies of electron transport in open quantum dots. *Phys: Condens Matter*, 1999;11:R413.
- [20] Friedman N, Kaplan A, Carasso D, Davidson N. Observation of Chaotic and Regular Dynamics in Atom-Optics Billiards. *Phys Rev Lett* 2001;86:1518.

- [21] Andersen MF, Kaplan A, Friedman N, Davidson N. Stable islands in chaotic atom-optics billiards, caused by curved trajectories. *J Phys B: At Mol Opt Phys* 2002;35:2183.
- [22] Kim Y-H, Barth M, Stöckmann H-J, Bird JP. Wave function scarring in open quantum dots: A microwave-billiard analog study. *Phys Rev B* 2002;65:165317.
- [23] Bird JP, Ferry DK, Akis R, Ochiai Y, Ishibashi K, Aoyagi Y, Sugano T. Periodic conductance fluctuations and stable orbits in mesoscopic semiconductor billiards. *Europhys Lett* 1996;35:529–34.
- [24] Kotelnikov IA, Popov SS, Romé M. Photon neutralizer as an example of an open billiard. *Phys Rev E* 2013;87:013111.
- [25] Harayama T, Shinohara S. Ray-wave correspondence in chaotic dielectric billiards. *Phys Rev E* 2015;92:042916.
- [26] Zanetti FM, Lyra ML, de Moura FABF, Luz MGEd. Resonant scattering states in 2D nanostructured waveguides: a boundary wall approach. *Phys B: At Mol Opt Phys* 2008;42:025402.
- [27] Nunes A, Zanetti FM, Lyra ML. Switching of transmission resonances in a two-channels coupler: A Boundary Wall Method scattering study. *Ann Phys* 2016;373:707–16.
- [28] Āawniczak M, Biaous M, Yunko V, Bauch S, Sirko L. Missing-level statistics and analysis of the power spectrum of level fluctuations of three-dimensional chaotic microwave cavities. *Phys Rev E*, 2018;98:012206.
- [29] Dietz B, Klaus T, Miski-Oglu M, Richter A, Wunderle M. Partial Time-Reversal Invariance Violation in a Flat, Superconducting Microwave Cavity with the Shape of a Chaotic Africa Billiard. *Phys Rev Lett* 2019;123:174101.
- [30] Leonel ED, Bunimovich LA. Suppressing Fermi Acceleration in a Driven Elliptical Billiard. *Phys Rev Lett* 2010;104:224101.
- [31] Costa DRD, Dettmann CP, de Oliveira JA, Leonel ED. Dynamics of classical particles in oval or elliptic billiards with a dispersing mechanism. *Chaos* 2015;25:033109.
- [32] Sieber M. Semiclassical transition from an elliptical to an oval billiard. *J Phys A: Math Gen* 1997;30:4563–96.
- [33] Sieber M. Semiclassical treatment of diffraction in billiard systems with a flux line. *Phys Rev E* 1999;60:3982.
- [34] Sieber M, Pavloff N, Schmit C. Uniform approximation for diffractive contributions to the trace formula in billiard systems. *Phys Rev E* 1997;55:2279.
- [35] Costa DRD, de Carvalho RE. Dynamics of a light beam suffering the influence of a dispersing mechanism with tunable refraction index. *Phys Rev E* 2018;98:022224.
- [36] Costa DRD, Dettmann CP, Leonel ED. Circular, elliptic and oval billiards in a gravitational field. *Commun Nonlinear Sci Numer Simulat* 2015;22:731–46.
- [37] Costa DRD, Oliveira DFM, Leonel ED. Dynamical and statistical properties of a rotating oval billiard. *Commun Nonlinear Sci Numer Simulat* 2014;19:1926–34.
- [38] Manchein C, Beims MW. Conservative generalized bifurcation diagrams. *Phys Lett A* 2013;377:789.
- [39] Dullin HR. Linear stability in billiards with potential. *Nonlinearity* 1998;11:151–73.
- [40] Barrio1 R, Blesa F, Serrano S. Fractal structures in the Hénon-Heiles Hamiltonian. *EPL*, 2008;82:10003.
- [41] Eckmann JP, Ruelle D. Ergodic theory of chaos and strange attractors. *Rev Mod Phys* 1985;57:617.